Relationship of mode transitions and standing waves in helicon plasmas

Mingyang WU (吴明阳)[1]**, Chijie XIAO** (肖池阶)[1,*]**, Xiaogang WANG** (王晓钢)[1,2,*]**,
Yue LIU** (刘悦)[3]**, Min XU** (许敏)[4]**, Chang TAN** (谭畅)[5,6]**, Tianchao XU** (徐田超)[1]**,
Xiuming YU** (余修铭)[1]**, Renchuan HE** (何任川)[1] **and Andong XU** (许安冬)[1]

[1] State Key Laboratory of Nuclear Physics and Technology, School of Physics, Fusion Simulation Center,
Peking University, Beijing 100871, People's Republic of China
[2] Department of Physics, Institute of Space Environment and Matter Science, Harbin Institute of
Technology, Harbin 150001, People's Republic of China
[3] Key Laboratory of Materials Modification by Laser, Ion and Electron Beams (Ministry of Education),
School of Physics, Dalian University of Technology, Dalian 116024, People's Republic of China
[4] Center for Fusion Science of Southwestern Institute of Physics, Chengdu 610041, People's Republic of China
[5] Shaanxi Key Laboratory of Plasma Physics and Applied Technology, Xi'an 710100, People's Republic of
China
[6] Xi'an Aerospace Propulsion Institute, Xi'an 710100, People's Republic of China

E-mail: cjxiao@pku.edu.cn and xgwang@hit.edu.cn

CrossMark

Abstract

Helicon wave plasma sources have the well-known advantages of high efficiency and high
plasma density, with broad applications in many areas. The crucial mechanism lies with mode
transitions, which has been an outstanding issue for years. We have built a fluid simulation
model and further developed the Peking University Helicon Discharge code. The mode
transitions, also known as density jumps, of a single-loop antenna discharge are reproduced in
simulations for the first time. It is found that large-amplitude standing helicon waves (SHWs) are
responsible for the mode transitions, similar to those of a resonant cavity for laser generation.
This paper intends to give a complete and quantitative SHW resonance theory to explain the
relationship of the mode transitions and the SHWs. The SHW resonance theory reasonably
explains several key questions in helicon plasmas, such as mode transition and efficient power
absorption, and helps to improve future plasma generation methods.

(Some figures may appear in colour only in the online journal)

1. Introduction

Producing high-density plasmas with high power efficiency is
the central issue in plasma research, with broad applications in
science and technology. Helicon wave plasma (HWP) sources
are well known for their advantages of high power efficiency
and high plasma density, as well as the feature of having no
internal electrode [1, 2]. They thus have important applications
in basic plasma research [3, 4], materials processing [5], cur-
rent drive in tokamaks [6–8], electric propulsion [9–11], and

many other areas. In particular, high density and high effi-
ciency plasmas can greatly improve the use of energy and
working media for better applications. The key to the high
density and high efficiency of helicon plasmas lies on the
transitions between various discharge modes, especially from
the inductive (H) mode to the wave (W) modes, with sig-
nificant density jumps [12, 13]. The H mode discharge exhibits
low density and low power absorption efficiency. As the dis-
charge power increases, the discharge will switch from H mode
to W modes, accompanied by a rapid increase in density and
power efficiency. Nevertheless, the physical mechanism of the
mode transition is still an outstanding issue [14, 15].

---

* Authors to whom any correspondence should be addressed.

Since Boswell discovered helicon plasmas in 1970 [16], their discharge mechanism has been studied extensively [14, 15, 17, 18]. Nevertheless, the calculated collisional absorption rate for helicon waves was much too low to explain the efficient ionization observed in experiments [16, 19]. Chen suggested that the Landau damping of the helicon waves possibly led to efficient power absorption [19]. On the other hand, however, experiments found that such Landau damping was unimportant to helicon plasmas [20]. Then, the strongly damped Trivelpiece-Gould (TG) wave was considered as the main heating mechanism [14, 21, 22]. However, the TG wave induced effects were expected to be important only for low dc magnetic fields and/or low plasma density [23, 24]. Nisoa *et al* further suggested a connection between high density and standing helicon waves (SHWs) [25, 26]. The presence of SHWs has been observed experimentally [13, 25–27], but the mechanism leading to the high density has not been clarified.

Clearly, the discharge mechanism in helicon plasmas has not been fully understood in previous studies. Thus there are still a few key issues to be resolved: (1) high efficient power absorption [28]; (2) mode transitions and different W modes [13]. There are also other questions to be answered, e.g., why W mode discharges can be realized by different antennas, such as helical, Nagoya, Boswell antennas, and even a single metal loop, etc [14]. In addition, the background magnetic field and measured densities are in agreement with the helicon wave dispersion relation [28]. Moreover, the lower the pressure is, the more pronounced the density jump is found in helicon discharges [13, 29].

Although many experiments have found density jumps [13, 26, 30, 31], direct simulation results are still lacking. The Peking University Helicon Discharge (PHD) code [32] has been developed to study the mechanism of helicon discharges. It is found in this work that the large-amplitude SHWs formed during the discharge processes are responsible for the mode transitions. The processes involved are as those of a resonant cavity for laser generation. The SHW resonance theory proposed in this work reasonably explains the key problems mentioned above. In addition, the SHW resonance theory can predict the conditions of density jumps and can be used to design HWP sources. Moreover, simulation results of the density jumps are presented for the first time. The simulations of the density jump and the theoretical analysis for the SHW resonance are presented as follows.

2. Mode transitions

Argon discharge processes are numerically studied by the PHD code. A single-fluid model of equations (1)–(5) is applied, with basic discharge processes, such as ionizations, transports, and power depositions. The electromagnetic waves in vacuum and plasma areas can be described by Maxwell's equations (1) and (2) and the generalized Ohm's law

equation (3) [1, 32].

$$\frac{\partial \boldsymbol{B}}{\partial t} = -\nabla \times \boldsymbol{E}, \tag{1}$$

$$\frac{\partial \boldsymbol{E}}{\partial t} = \frac{1}{\mu_0 \varepsilon_0 \varepsilon_r}(\nabla \times \boldsymbol{B} - \mu_0(\boldsymbol{J}_a + \boldsymbol{J}_p)), \tag{2}$$

$$\frac{\partial \boldsymbol{J}_p}{\partial t} = \frac{e^2 n_e}{m_e}E - \frac{e}{m_e}\boldsymbol{J}_p \times \boldsymbol{B}_0 - \nu_e \boldsymbol{J}_p, \tag{3}$$

where $\boldsymbol{J}_a$, $\boldsymbol{J}_p$ and $\boldsymbol{B}_0$ are current densities of the antenna and the plasma, and the background magnetic field, respectively. The frequency of helicon wave is much higher than the lower hybrid frequency, so that ion motions can be neglected in equation (3). Equations for the plasma density and the electron temperature are

$$\frac{\partial n}{\partial t} + \nabla \cdot \boldsymbol{\Gamma} = S, \tag{4}$$

$$\frac{3}{2}\frac{\partial}{\partial t}(nT_e) + \nabla \cdot \boldsymbol{q}_e = p_p - H_i S, \tag{5}$$

where n is the plasma density. For the single-fluid model, we have $n = n_i = n_e$, where n_i and n_e are the argon ion density and electron density, respectively. Also, the closure for particle flux $\boldsymbol{\Gamma}$ and electron energy flux $\boldsymbol{q}_e$ are written as

$$\boldsymbol{\Gamma} = D_{a\perp}\nabla_\perp n\,\boldsymbol{e}_\perp + D_a\nabla_\parallel n\,\boldsymbol{e}_\parallel, \tag{6}$$

$$\boldsymbol{q}_e = -\frac{3}{2}n(D_{a\perp}\nabla_\perp T_e\boldsymbol{e}_\perp + D_a\nabla_\parallel T_e\boldsymbol{e}_\parallel) + \frac{5}{2}T_e\boldsymbol{\Gamma}, \tag{7}$$

where subscripts $\parallel$ and $\perp$ represent the parallel and perpendicular directions to the magnetic field. The power deposition density p_p in the plasma is $p_p = \boldsymbol{J}_p \cdot \boldsymbol{E}$. The total plasma power absorption P_t is obtained by spatially integrating and periodically averaging p_p, i.e.,

$$P_t = \frac{1}{T_{rf}}\iiint\int_{t_0}^{t_0+T_{rf}} rp_p\,\mathrm{d}t\mathrm{d}r\mathrm{d}\theta\mathrm{d}z, \tag{8}$$

where T_{rf} is the period of the radio frequency (RF). The ionization term $S = k_i n_n n_e$ is only for the ground state atom ionization and H_i is the first ionization energy. The calculation of the ambipolar diffusion coefficients D_a and $D_{a\perp}$ and other parameters can be found in [32, 33]. The boundary conditions on the plasma-wall interface are

$$\boldsymbol{\Gamma} = \frac{1}{4}n v_{e,th}\boldsymbol{e}_n, \tag{9}$$

$$\boldsymbol{q}_e = 2k_B T_e \boldsymbol{\Gamma}_e, \tag{10}$$

where $\boldsymbol{e}_n$ is the normal vector to the wall from the plasma, and $v_{e,th}$ is the electron thermal velocity at the wall. Perfect conductor boundary conditions are used for the sidewall and both end plates.

To compare the density jumps of the single-loop antenna between simulations and experiments, we use a configuration similar to that of [26], but with a slightly different antenna size. The configuration is shown in figure 1. In the cylindrical coordinate, the entire computational space is in the range of $r = [0\ R_D]$ and $z = [0\ Z_D]$, with $R_D = 2.75$ cm and $Z_D = 65$ cm, respectively. The radial and axial distributions of the
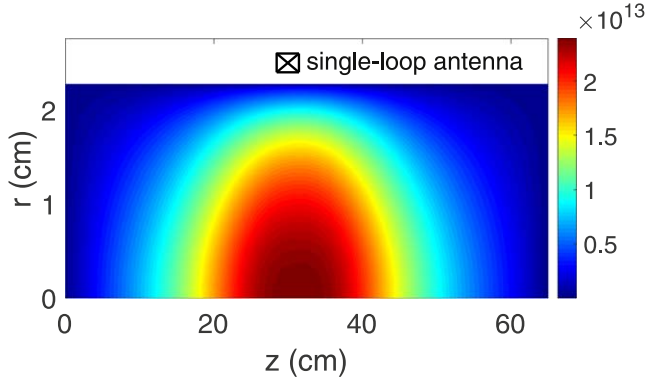
Figure 1. Schematic diagram of the simulation domain, where the contour is the steady-state electron density n_e in cm^{-3} for the parameters of (3000 W, 1.06 Pa, 237 G).

Figure 2. The variation of steady-state density with power, where the experimental data in solid black dots are from [26].
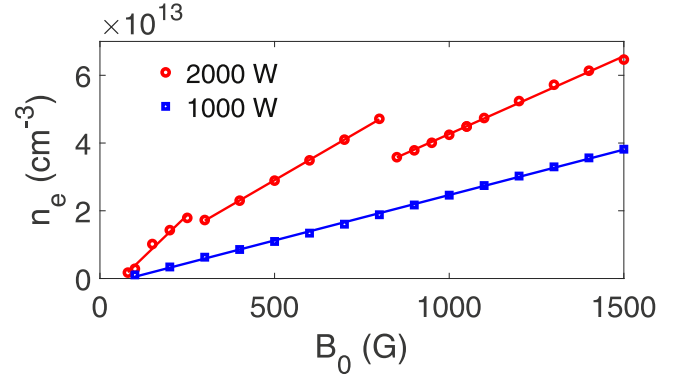

Figure 3. The variation of steady-state density with the applied magnetic field, where the solid lines are linear fits of the simulated data. The argon pressure is 0.3 Pa.
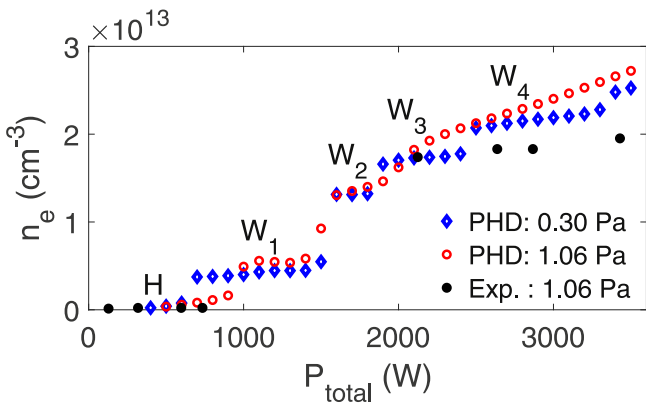

Figure 4. Evolution of the maximum electron density for different RF powers, with parameters of (237 G, 0.3 Pa).

plasma are in the range of $r = [0\ R_p]$ with $R_p = 2.25$ cm and $z = [0\ Z_D]$. The positions of the single-loop antenna with a width of 0.2 cm radially and 3 cm axially are $r_a = 2.4$ cm and $z_a = 32.5$ cm, respectively. The total input power P_{total} is equal to the electron power absorption P_t plus the Joule heat of the antenna $I_a^2 R_a$, i.e., $P_{total} = P_t + I_a^2 R_a$, where $R_a = 0.1\ \Omega$ is the antenna resistance. The antenna current amplitude I_a is adjusted to the total plasma power absorption P_t to maintain a constant total power P_{total}. The antenna current is taken as $\boldsymbol{J}_a = \frac{I_a(r,z,t)}{S_a} \sin(2\pi f t)\boldsymbol{e}_\theta$ with a frequency $f = 13.56$ MHz, where S_a is the cross-sectional area of the antenna.

When the initial density n_{ini} is low, the plasma density is relatively low due to the capacitive discharge. Thus, the initial density is set as $n_{ini} = 10^{11}$ cm^{-3} to discuss the transition of H to W mode. A uniform background magnetic field with a magnitude of $B_0 = 237$ G is applied. The maximum plasma density at the steady state versus the power is shown in figure 2. The plasma density was measured by the ion saturation current of Langmuir probes at $r = 0$ and $z = 28.5$ cm [26]. Significant jumps in the density are found, especially with the neutral pressure of $p_n = 0.3$ Pa. These modes are named as H, W1, W2, W3, W4 in order, respectively, where W1–W4 are various helicon wave modes.
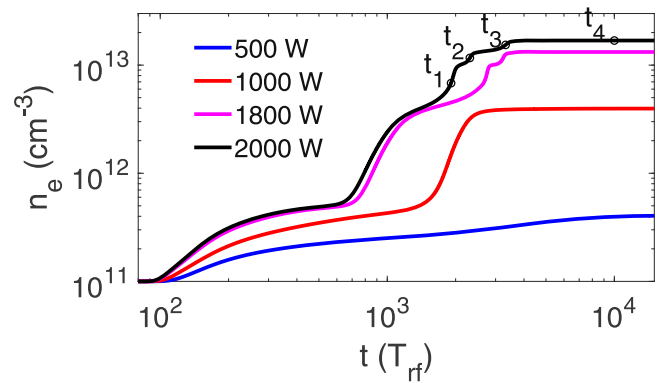
We further discuss the density jumps with the applied magnetic field strengths. Figure 3 shows the variation of steady-state density with the applied magnetic field. It can be seen that the density and magnetic field show a good linear relationship in a certain magnetic field range. In the dispersion relation of helicon waves, if the wave number is assumed to be a constant, the density and the magnetic field are linear as well. Conversely, if the density and the magnetic field show a linear relationship, it can be inferred that the wave number is the same in that magnetic field range. The subsequent analysis in section 3 points out that a wave number corresponds to a wave mode discharge. In the 2000 W power discharge, three line segments with different slopes appear, and we infer that they are three different W mode discharges. In the 1000 W power discharge, the discharges of different magnetic fields are the same W mode. Further analysis is to be carried out in the next article.

For the W mode discharges, it is found that the plasma density undergoes the second and/or even multiple jumps over time, as shown in figure 4; the same as the results in [32].

A clear standing wave structure appears at the moments of t_1, t_2 and t_3, shown in figure 5. The density jumps at different moments correspond to different axial mode numbers. The simulated wavelength of these moments is then compared with the dispersion relation of helicon waves in equation (13), where the radial wave number is $k_r = Z_n/r_D$. The simulated
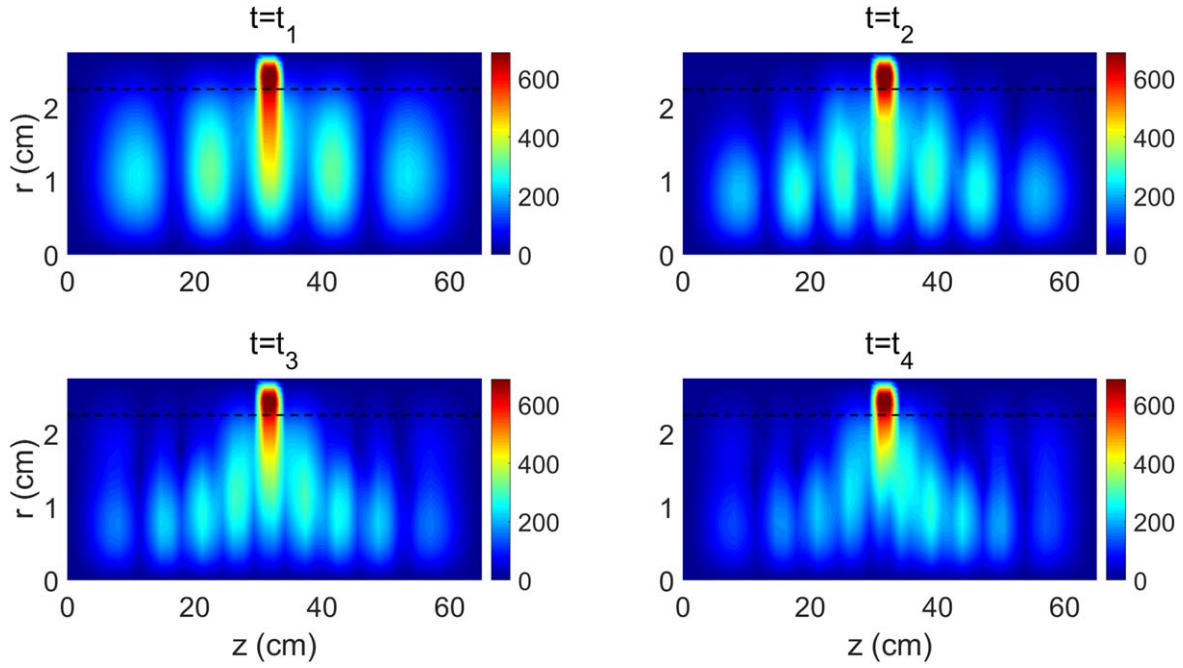
Figure 5. The distribution of the amplitude of the azimuthal electric field E_θ with units in V/m at different moments, where $t_1 - t_4$ are marked in figure 4 and the discharge parameters are (2000 W, 237 G, 0.3 Pa).

wavelengths at moments t_1, t_2 and t_3 are 19.5 cm, 14.1 cm and 9.8 cm, respectively, and the dispersion relations for the helicon waves are given as 18.3 cm, 11.2 cm and 8.8 cm, respectively. The simulated results are close to the analytical dispersion relationship. The error comes from the inhomogeneity of the density. Therefore, we conclude that these standing waves are SHWs. The SHWs are observed just before these jumps and disappear at the steady state (similar to the figure 9 in [32]), as shown in figure 5. The reason is that the large-amplitude SHWs corresponding to the standing wave condition lead to a large amount of ionization, which makes the density increase and thus the standing wave condition fails, i.e., the large-amplitude SHWs disappear. When the discharge has reached the W mode, the high density leads to a high enough collision rate, and as a result, the partial SHWs can also maintain a steady-state discharge. Therefore, only partial standing waves are often observed in steady-state measurements [13, 25, 26, 34]. Rather than at the steady state, we thus suggest we should seek to detect the transition between H and W modes, and different W modes. The PHD simulation results closely fit the experimental results, as shown in figure 2.

3. Physical mechanism

To further understand the mode transition, we then analyze the mechanism of the high electromagnetic power absorption in the helicon plasmas. That is, the equations (1)–(3) are studied in focus. Similar to Chen's analytical solution in cylindrical coordinates [19], with the polarization current and the electron inertia term neglected in equations (2) and (3), we

have the azimuthal electric field

$$E_\theta = -\frac{\omega}{k_z}\frac{\mathrm{i}C_3}{T^2}\left(\frac{m}{r}\alpha J_m(Tr) - k_z J'_m(Tr)\right) \\ \times \exp(im\theta + ik_z z - \mathrm{i}\omega t), \tag{11}$$

where J_m is the mth order Bessel function and $T^2 = \alpha^2 - k_z^2$ is the transverse wavenumber. The quantity α is defined as $\alpha = \frac{\omega}{k_z}\frac{\mu_0 e n_e}{B_0}$ and C_3 is an integration constant. For simplicity, we analyze the azimuthal mode with the mode number $m = 0$. The analysis procedure for other modes ($m \neq 0$) is similar to that for $m = 0$. As an example, the simulation of the helical antenna with $m = 1$ has been carried out and verified to be similar to $m = 0$. Then, for $m = 0$, equation (11) becomes

$$E_\theta = C_3\frac{\mathrm{i}\omega}{T^2}J_1(Tr)\exp(ik_z z - \mathrm{i}\omega t). \tag{12}$$

A perfect conductor boundary condition, $E_\theta(a) = 0$, is then applied to the plasma radial boundary $r = a$. The dispersion relation can thus be written as a function of plasma parameters,

$$\frac{\omega\mu_0 e n_e}{B_0} = k_z\sqrt{k_z^2 + \left(\frac{Z_n}{a}\right)^2}, \tag{13}$$

where Z_n is the nth root of $J_1(x) = 0$ with n being the radial mode number. The analytical solution (equations (12) and (13)) can be used for cross-validation for simulation results.

Equations (1)–(3) are numerically solved by the PHD code [32], in which the alternating-direction-implicit finite-difference time-domain (ADI-FDTD) method is used to improve computational efficiency [35, 36]. The schematic diagram of the simulation domain, which has analytic solutions, is shown in figure 6. In the cylindrical coordinate
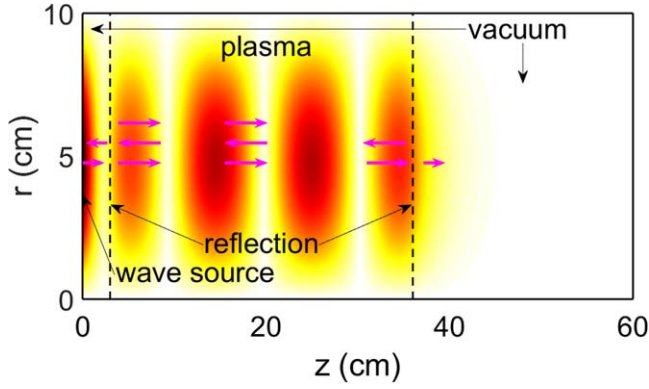
Figure 6. Schematic diagram of the simulation domain and the distribution of SHWs, where the contour is the amplitude of E_θ for $n_e = 8.22 \times 10^{12}$ cm^{-3}, and the pink arrows indicate the propagation of helicon waves with reflections at both dashed lines.

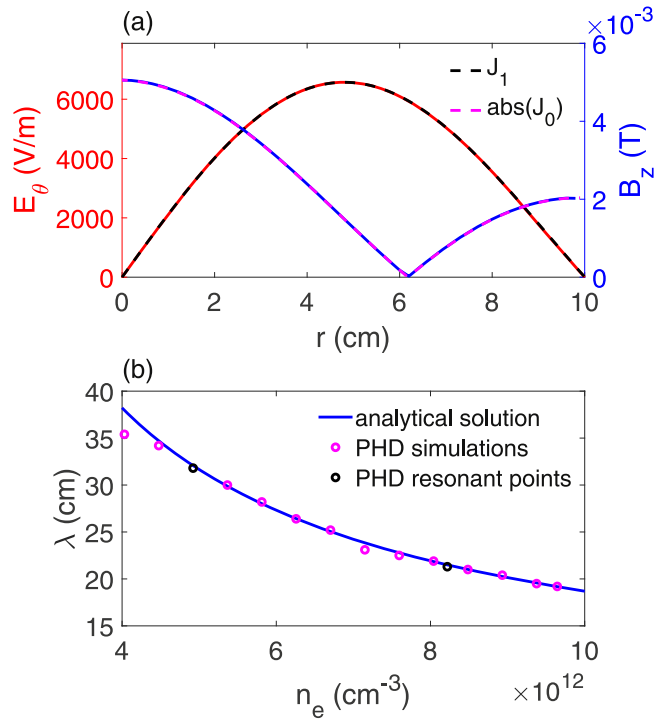**Figure 7.** (a) the amplitude of $E_\theta(r)$ and $B_z(r)$ (point B in figure 8(a)) at $z = 15$ cm fitted by the Bessel function $J_1(r)$ and $J_0(r)$, respectively, and (b) the wavelength λ of helicon waves for the simulation and the analytical solution.

system, the entire computational space is in $r = [0\ a]$ radially and $z = [0\ Z_0]$ axially, with $a = 10$ cm and $Z_0 = 60$ cm. The distribution of the plasma is in the area of $r = [0\ a]$ radially, and $z = [Z_{p1}\ Z_{p2}]$ axially, with $Z_{p1} = 3$ cm and $Z_{p2} = 36$ cm. With no loss of generality, the plasma region is assumed with a fixed and uniform density, while all other regions are vacuum. The background magnetic field is a uniform magnetic field with a magnitude of $B_0 = 1000$ G, and the neutral pressure is $p_n = 0.3$ Pa.

The wave-driven boundary conditions are applied as $E_\theta(r,\ t) = E_0 J_1\!\left(\frac{z_1}{a} r\right) \sin \omega t$ and $E_r = E_z = 0$ at $z = 0$, with a
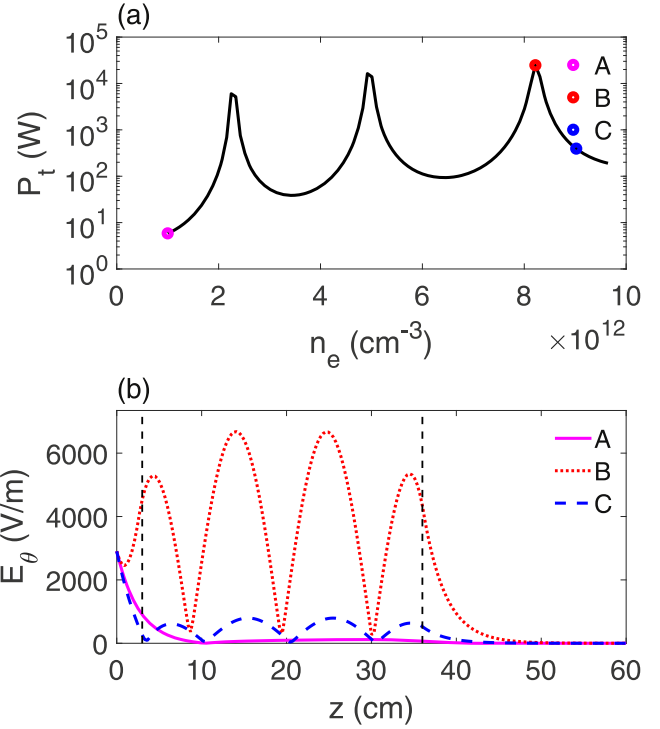

Figure 8. (a) The dependence of P_t on n_e. (b) The amplitude of $E_\theta(z)$ at $r = \frac{R_0}{2}$ with three different densities, respectively, corresponding to Points A, B and C in (a).

wave-driven intensity $E_0 = 5000$ V m^{-1} and a frequency $f = \frac{\omega}{2\pi} = 13.56$ MHz. Perfect conductor boundary conditions are used at $r = a$ and $z = Z_0$.

Both the electromagnetic field amplitude and the cycle-averaged power deposition are in steady state after $\sim 100 T_{rf}$ for a specific n_e. Figure 7 shows the azimuthal electric field $E_\theta(r)$, the axial magnetic field $B_z(r)$ and the wavelength $\lambda = \frac{2\pi}{k_z}$ at $t = 200 T_{rf}$ (steady state), for simulations and analytical solutions. Figure 7(a) shows that the radial structures of E_θ and B_z fit the Bessel functions very well. Kyeong-Koo Chi *et al* also observed that the radial $B_\parallel$ had a form of the Bessel function [13]. In fact, simulation results at different densities and positions in our work always show a good fit with the Bessel function-like analytical solution. The wavelengths shown in figure 7(b) are calculated from the axial structure of E_θ (shown in figure 8(b)). Thus, one can see that the simulated dispersion relation matches well with the theoretical solution. According to figure 7, the numerical and theoretical solutions mutually verify the conclusion that the dominant waves in the system are the helicons.

Figure 8(a) shows the dependence of P_t on n_e, with three peaks of two orders of magnitude higher than the background. We refer to these peaks as resonances. The resonant and non-resonant $E_\theta(z)$ at $r = \frac{R_0}{2}$ are shown in figure 8(b). It can be seen that at a low density (curve A), E_θ decays exponentially along the axis. In the resonance, we have the curve B for the large-amplitude SHW, where a clear standing wave appears and the maximum amplitude of E_θ in the plasma considerably

exceeds the wave source. In non-resonant and high-density conditions (curve C), the SHW also appears, but with an amplitude significantly lower than that of curve B. It should be noticed that curves A and B in figure 8(b) are very similar to the experiment results in figure 9 of Motomura *et al* [37].

The power deposition can be written as $p_p = \boldsymbol{J}_p \cdot \boldsymbol{E} = |\boldsymbol{J}_p||\boldsymbol{E}| \cos \phi$, where $|\boldsymbol{J}_p|$, $|\boldsymbol{E}|$ and ϕ are the amplitudes of $\boldsymbol{J}_p$ and $\boldsymbol{E}$, and the phase shift between $\boldsymbol{J}_p$ and $\boldsymbol{E}$, respectively. The simulation then reveals the dependence of $|\boldsymbol{J}_p|$ and $|\boldsymbol{E}|$ on n_e with peaks similar to that in figure 8(a), while the dependence of $\cos \phi$ on n_e is almost monotonically increased by $\sim 40\%$. Furthermore, $|\boldsymbol{J}_p|$ is approximately proportional to $|\boldsymbol{E}|$. Therefore, we can predict that the resonance absorption peaks in figure 8(a) are due to the wave energy $|\boldsymbol{E}|^2$. The simulation results show the large-amplitude SHWs do indeed result in the peaks as $|\boldsymbol{E}|^2$ varies with n_e.

Thus, the numerical simulations predict that the large-amplitude SHWs lead to efficient power absorption and mode transitions. The formation mechanism of the large-amplitude SHWs is now discussed. The helicon wave is weakly damped and able to propagate over a long distance in the plasma. The wave is then reflected at the plasma boundary, with a mechanism described later, and superimposed to form SHWs, as shown in figure 6. When the SHW resonance condition,

$$L_z = \frac{N}{2} \lambda (N = 1, \ 2, \ 3 \ \ldots), \tag{14}$$

is satisfied, where L_z is the axial length of the plasma column, the wave amplitude is coherently rising and the large-amplitude SHWs are formed to trigger a mode transition. The processes involved are as those for a resonant cavity to generate a laser. This SHW resonance theory is applicable to lots of helicon waves with different m, usually determined by helical, Nagoya, Boswell and single-loop antennas. Although the wavelengths are different for different m helicon waves, their SHW resonance conditions are all determined by equation (14). The peak of power absorption occurs when this condition is satisfied. In applied discharges, there are usually two quantum numbers, the axial mode number N and the radial mode number n. The combination of these two quantum numbers yields different W modes. Multiple W modes observed in experiments [13] can be interpreted by different (N, n) modes. In addition, the SHW resonance condition requires a density higher than a threshold (corresponding to $N = 1$ and $n = 1$), which is the reason why the W modes cannot be reached at low power. It can be inferred that the longer the plasma column or the lower the magnetic field is, the lower the hopping power will be. In addition, under the same other conditions, the damping rate of the helicon wave does not change as L_z increases. Therefore, the distance the wave travels does not change. As L_z increases, the number of helicon waves traveling through the plasma decreases, resulting in a decrease in the amplitude of the superimposed wave and a decrease in the peak value of power deposition. In the discharge processes, an increase in L_z leads to less obvious density jumps. Nevertheless, the increase in L_z within a certain range may not reduce the power absorption
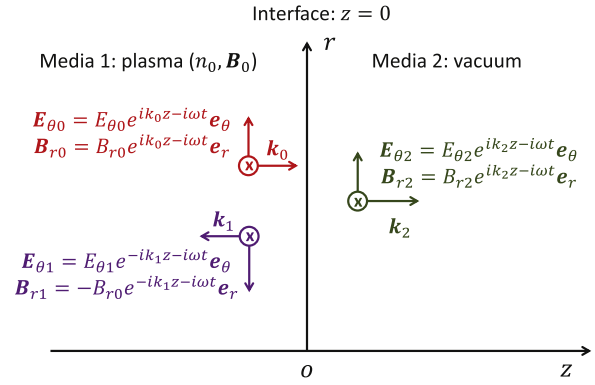

Figure 9. Schematic diagram of the reflection of a helicon wave, where the incident, refracted, and reflected waves are marked in red, green and purple, respectively.

efficiency of the W mode discharge, because the efficient power absorption mechanism of standing wave resonance is still effective. In summary, an increase in L_z will result in 3 effects, including (1) a less obvious density jump, (2) an uncertain change in power efficiency and (3) a reduction in the power threshold required for the W mode. Although the plasma density and the background magnetic field are not uniform in general, the physical process is nevertheless approximately the same.

Reflection is necessary for the formation of SHWs. The metal end plate can easily reflect helicon waves. On the insulated end plates, it is found that with a high plasma density and a strong magnetic field, the helicon wave can also be reflected by the insulated end plates almost completely. The analysis is as follows.

Figure 9 shows a helicon wave propagating parallel to the z-axis from medium 1 (the plasma with $\boldsymbol{B}_0 = B_0 \boldsymbol{e}_z$) to medium 2 (the vacuum). The generated azimuthal electric field E_θ and radial magnetic field B_r are then analyzed. The interface $(z = 0)$ separating the two media is an insulated end plate. The subscripts of incident, reflected, and refracted waves are marked as 0, 1 and 2, respectively. The relation between the magnetic and electric fields is written as

$$E_{\theta 0} = \frac{\omega}{k_0} B_{r0}, \ \ E_{\theta 1} = \frac{\omega}{k_1} B_{r1}, \ \ E_{\theta 2} = \frac{\omega}{k_2} B_{r2}. \tag{15}$$

Considering the strong magnetic field and high plasma density, the wavenumbers k_0 and k_1 in the plasma are much larger than those in the vacuum, k_2, i.e.,

$$k_0 = k_1 \gg k_2. \tag{16}$$

The insulation boundary condition is applied as

$$\boldsymbol{e}_n \times (\boldsymbol{E}_2 - \boldsymbol{E}_1) = 0, \tag{17}$$

$$\boldsymbol{e}_n \times (\boldsymbol{H}_2 - \boldsymbol{H}_1) = 0, \tag{18}$$

where $E_1 = E_{\theta 0} + E_{\theta 1}$, $E_2 = E_{\theta 2}$, $H_1 = \frac{B_{r0}}{\mu_0} + \frac{B_{r1}}{\mu_0}$, $H_2 = \frac{B_{r2}}{\mu_0}$. Combining equations (15)–(18), the amplitudes of the reflected and refracted waves are obtained,

$$E_{\theta 1} = \frac{k_0 - k_2}{k_0 + k_2} E_{\theta 0} \approx E_{\theta 0}, \tag{19}$$

$$E_{\theta 2} = \frac{2k_0}{k_0 + k_2} E_{\theta 0} \approx 2E_{\theta 0}. \tag{20}$$

The amplitude of the reflected wave is approximately equal to that of the incident wave, indicating the wave to be mostly reflected. The amplitude of the refracted wave is nearly twice that of the incident wave, while the energy of the refracted wave is derived from the magnetic energy in the incident wave. The reason for the almost total reflection is that the wave number in the plasma under a strong magnetic field is much larger than that in the vacuum, i.e. equation (16). The reflection on the insulated end plate is then consistent with the experimental results in [37] (figure 11), where the standing wave structures were observed for both conductor and insulated end plates.

Both simulations and experiments show that the lower the pressure is, the more pronounced the jumps are [13, 29]. The reason is that a lower pressure leads to a smaller collision frequency and damping rate of the wave. Thus, the helicon wave travels longer, the superimposed electric field intensity is bigger, and the power absorption peaks become narrower and higher. As a result, the discharge pattern jumps significantly at low pressure. In addition, as the steady-state density exceeds 10^{13} cm^{-3}, the density jump becomes less pronounced due to the high collision frequency.

4. Conclusion

In conclusion, the density jumps of a single-loop antenna discharge are reproduced in simulations for the first time and a complete and quantitative SHW resonance theory is presented in this paper. It is seen that the large-amplitude SHWs are responsible for the mode transitions, similar to those of a resonant cavity for laser generation. The SHW resonance theory reasonably explains the key problems of efficient power absorption and mode transitions. In addition, the analysis is independent of the antenna type. Therefore, the SHW resonance theory can be applied to plasmas excited by different types of helicon antennas. Moreover, the SHW resonance theory can also interpret: (1) the background magnetic field and measured densities are in agreement with the helicon wave dispersion relation; (2) the lower the pressure is, the more pronounced the density jump will be in helicon discharges. Finally, the mechanism of standing wave resonance can also be applied to other reflective or periodic systems to improve their efficiency, such as wave drive/heating in tokamak plasmas.

References

[1] Chen F F 1995 Helicon plasma sources *High Density Plasma Sources* ed O A Popov (Park Ridge: William Andrew)
[2] Longmier B W *et al* 2011 *Plasma Sources Sci. Technol.* **20** 015007
[3] Manz P *et al* 2011 *Phys. Rev. Lett.* **107** 195004
[4] Xiao C J *et al* 2016 *Rev. Sci. Instrum.* **87** 11D610
[5] Bose D, Govindan T R and Meyyappan M 2003 *IEEE Trans. Plasma Sci.* **31** 464
[6] Petrzilka V and Tataronis J A 1994 *Plasma Phys. Control. Fusion* **36** 1027
[7] Lau C *et al* 2018 *Nucl. Fusion* **58** 066004
[8] Yang Y Q *et al* 2020 *J. Fusion Energy* **39** 521
[9] Squire J P *et al* 2006 *Thin Solid Films* **506–507** 579
[10] West M D, Charles C and Boswell R W 2009 *J. Phys. D: Appl. Phys.* **42** 245201
[11] Takahashi K *et al* 2011 *Phys. Rev. Lett.* **107** 235001
[12] Lieberman M A and Boswell R V 1998 *J. Phys. IV France* **8** Pr7–r145
[13] Chi K K, Sheridan T E and Boswell R W 1999 *Plasma Sources Sci. Technol.* **8** 421
[14] Chen F F 2015 *Plasma Sources Sci. Technol.* **24** 014001
[15] Isayama S, Shinohara S and Hada T 2018 *Plasma Fusion Res.* **13** 1101014
[16] Boswell R W 1970 *Phys. Lett.* A **33** 457
[17] Boswell R W 1975 *Nature* **258** 58
[18] Boswell R W and Chen F F 1997 *IEEE Trans. Plasma Sci.* **25** 1229
[19] Chen F F 1991 *Plasma Phys. Control. Fusion* **33** 339
[20] Chen F F and Blackwell D D 1999 *Phys. Rev. Lett.* **82** 2677
[21] Arnush D and Chen F F 1998 *Phys. Plasmas* **5** 1239
[22] Blackwell D D *et al* 2002 *Phys. Rev. Lett.* **88** 145002
[23] Borg G G and Boswell R W 1998 *Phys. Plasmas* **5** 564
[24] Chen F F and Arnush D 1997 *Phys. Plasmas* **4** 3411
[25] Nisoa M, Sakawa Y and Shoji T 1999 *Jpn. J. Appl. Phys.* **38** L777
[26] Nisoa M *et al* 2000 *Jpn. J. Appl. Phys.* **39** L429
[27] Light M I *et al* 1995 *Phys. Plasmas* **2** 4094
[28] Boswell R W 1984 *Plasma Phys. Control. Fusion* **26** 1147
[29] Zhang T L *et al* 2020 *Plasma Sci. Technol.* **22** 085405
[30] Ellingboe A R and Boswell R W 1996 *Phys. Plasmas* **3** 2797
[31] Franck C M, Grulke O and Klinger T 2003 *Phys. Plasmas* **10** 323
[32] Wu M Y *et al* 2021 *Plasma Sci. Technol.* **23** 085002
[33] Chabert P and Braithwaite N 2011 *Physics of Radio-Frequency Plasmas* (Cambridge: Cambridge University Press)
[34] Guittienne P *et al* 2021 *Plasma Sources Sci. Technol.* **30** 075023
[35] Yuan C H and Chen Z H 2002 *IEEE Trans. Microw. Theory Tech.* **50** 2401
[36] Chen H L *et al* 2007 *IEEE Microw. Wirel. Compon. Lett.* **17** 304
[37] Motomura T *et al* 2012 *Phys. Plasmas* **19** 043504